Magnetic and electrical properties of (Pu,Lu)Pd$_3$

M. D. Le[*]

Helmholtz-Zentrum Berlin für Materialen und Energie, Hahn-Meitner-Platz 1, D-14109 Berlin, Germany

K. A. McEwen

*Department of Physics and Astronomy, and London Centre for Nanotechnology, University College London,
WC1E 6BT, London, United Kingdom*

E. Colineau, J.-C. Griveau, and R. Eloirdi

Joint Research Centre, Institute for Transuranium Elements, European Commission, Postfach 2340, D-76125 Karlsruhe, Germany

We present measurements of the magnetic susceptibility, heat capacity, and electrical resistivity of Pu$_{1-x}$Lu$_x$Pd$_3$, with $x=0$, 0.1, 0.2, 0.5, 0.8, and 1. PuPd$_3$ is an antiferromagnetic heavy fermion compound with $T_N=24$ K. With increasing Lu doping, both the Kondo and Ruderman-Kittel-Kasuya-Yosida interaction strengths fall, as judged by the Sommerfeld coefficient γ and Néel temperature T_N. Fits to a crystal-field model of the resistivity also support these conclusions. The paramagnetic effective moment μ_{eff} increases with Lu dilution, indicating a decrease in the Kondo screening. In the highly dilute limit, μ_{eff} approaches the value predicted by intermediate coupling calculations. In conjunction with an observed Schottky peak at ~60 K in the magnetic heat capacity, corresponding to a crystal field splitting of ~12 meV, a mean-field intermediate coupling model with nearest-neighbor interactions has been developed.

I. INTRODUCTION

The AnPd$_3$ series of compounds, with $An=$U, Np, or Pu, are rare examples of actinide intermetallic compounds in which the $5f$ electrons are well localized around the ionic sites. UPd$_3$ is a very interesting compound which exhibits four quadrupolar ordered phases below 8 K (Ref. [1]) while there are indications that NpPd$_3$ may also show quadrupolar order at low temperatures.[2] These two compounds crystallize in the double-hexagonal close-packed structure, in contrast to PuPd$_3$ which adopts the AuCu$_3$ structure, with lattice parameter $a=4.105$ Å. This reflects the increasing localization of the $5f$ electrons as shown by recent photoelectron spectroscopy measurements.[3]

Early measurements of the bulk properties and neutron-diffraction studies[4] show it to be antiferromagnetic, with a transition temperature ~24 K, and a G-type structure, where nearest-neighbor moments are aligned antiparallel. The same study found that the high-temperature resistivity shows a Kondo-type behavior, increasing with decreasing temperature. This behavior, together with a high Sommerfeld coefficient deduced from recent heat capacity measurements,[5] led us to make a further investigation of the properties of PuPd$_3$.

Our aim has been to study how the competition between the Kondo effect and the Ruderman-Kittel-Kasuya-Yosida (RKKY) exchange interaction affects the physical properties of this compound. This may be accomplished by doping with a nonmagnetic ion, which increases the distance between localized f electrons and hence decreases the RKKY interaction. Finally, the single-ion properties of the Pu ion may be investigated in the highly dilute limit.

In this work, we present in Sec. II the experimental details and in Sec. III the measurements of the magnetic susceptibility and heat capacity of Pu$_{1-x}$Lu$_x$Pd$_3$. These measurements are then analyzed using a localized moment mean field

model in Sec. IV. Finally, Sec. V presents measurements of the electrical resistivity and Hall coefficient of Pu$_{1-x}$Lu$_x$Pd$_3$, which are assessed in terms of a simple crystal-field model.

II. EXPERIMENTAL DETAILS

Polycrystalline samples of PuPd$_3$, LuPd$_3$, and Pu$_{1-x}$Lu$_x$Pd$_3$, with $x=0.1$, 0.2, 0.5, and 0.8, were produced at ITU by arc melting appropriate amounts of the constituent elements under a high-purity argon atmosphere on a water-cooled copper hearth, using a Zr getter. The AuCu$_3$ structure was confirmed by x-ray diffraction for each sample, and the lattice parameters are shown in Fig. 1. The data show a linear dependence of the lattice parameter with increasing Lu dilu-
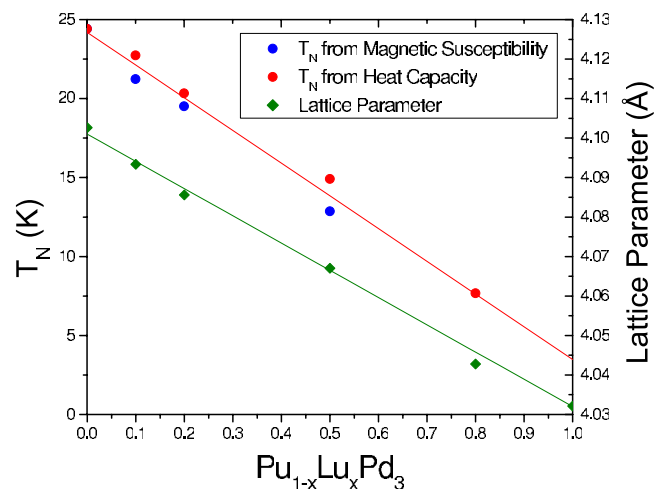

FIG. 1. (Color online) Lattice parameters and transition temperatures for Pu$_{1-x}$Lu$_x$Pd$_3$.

TABLE I. Transition temperatures and other parameters derived from the magnetic susceptibility and heat capacity of $Pu_{1-x}Lu_xPd_3$.

Composition	T_N (K)		$\gamma^{\pm}$ (mJ mol^{-1} K^{-2})		θ_D (K)	μ_{eff} (μ_B Pu^{-1})	θ_{CW} (K)
	C_p	χ	$T > T_N$	$T < 8$ K	$T > T_N$		
$PuPd_3$	24.4(3)	24.9(4)		75(1)	306(19)	1.02(1)	−39.9(1)
$Pu_{0.9}Lu_{0.1}Pd_3$	22.7(4)	22.5(1)		133(8)	304(18)	0.97(2)	−15.8(2)
$Pu_{0.8}Lu_{0.2}Pd_3$	20(1)	19.5(1)		221(14)	280(6)	0.97(2)	−7.5(2)
$Pu_{0.5}Lu_{0.5}Pd_3$	15(1)	12.8(1)	183(36)	289(10)	270(10)	1.15(2)	1.8(1)
$Pu_{0.2}Lu_{0.8}Pd_3$	7(2)		99(49)	170(5)	257(13)	1.25(1)	−7.2(2)
$LuPd_3$				3.5(5)	291(12)		

tion, in accordance with Vegard's Law, which also confirms the stoichiometry of the samples. In addition, there also appears to be a linear dependence of the transition temperature, T_N, with doping. These temperatures were determined from magnetic susceptibility and heat capacity measurements described in the next section. At T_N there is a maximum in the susceptibility, χ, and hence this temperature was determined by numerically differentiating the data to find $\frac{d\chi}{dT} = 0$. In the heat capacity, C_p, there is a lambda step at T_N, which was determined by differentiating the data to find the minima of $\frac{dC_p}{dT}$. The values of T_N deduced from these two measurements are in close agreement whereas the inflexion points of the resistivity data do not correlate with T_N as determined from χ or C_p. Nevertheless, the resistivity inflexion points show the same decreasing trend with Lu doping as T_N. Errors in T_N quoted in Table I were determined by the width in temperature of the lambda step for C_p or the step in $\frac{d\chi}{dT}$.

The magnetization and susceptibility were measured using a superconducting quantum interference device magnetometer (Quantum Design magnetic property measurement system (MPMS)-7) while the heat capacity was determined by the hybrid adiabatic relaxation method in a Quantum Design physical property measurement system (PPMS)-9 for $PuPd_3$ and $LuPd_3$, and in a PPMS-14 for $Pu_{1-x}Lu_xPd_3$. Small samples with mass less than 5 mg were used for the heat capacity measurements so that the decay heat does not significantly affect the measurements. The x-ray diffraction, magnetization, and heat capacity measurements were made immediately after the preparation of samples in order to minimize the effects of radiation damage.

Finally, thin parallel-sided samples of each composition were extracted, polished and mounted for electrical transport measurements. As these measurements were made some three months after synthesis, we observed significant radiation damage which manifested in a high-residual resistivity at low temperatures. This prompted us to anneal the samples at 800 °C for 12 h, and to remeasure the electrical transport properties. The remeasured data is presented in Sec. V.

III. MAGNETIZATION AND HEAT CAPACITY MEASUREMENTS

A. Magnetization

Figure 2 shows the magnetization at 2 K, which shows

that the Pu-rich compositions are not saturated at 7 T. This is not surprising because we expect a $J = 5/2$ ion to be saturated at a field $\gtrsim 100$ T, when the splitting between the lowest two CF levels is $\gg 2$ K. The magnetization of $Pu_{0.2}Lu_{0.8}Pd_3$ shows some evidence of saturation, however. The magnetic susceptibility is shown in Fig. 3, and the inverse susceptibility in Fig. 4. The data in the paramagnetic phase above the Néel temperature are well fitted by a modified Curie-Weiss Law

$$\frac{M}{H} = \frac{N\mu_{eff}^2\mu_B^2}{3k_B}\frac{1}{T - \theta_{CW}} + \chi_0(H), \quad (1)$$

where N is the number of Pu atoms in the compound, and θ_{CW} is the paramagnetic Curie temperature. We recall that in the Weiss mean-field theory, $(-\theta_{CW})\theta_{CW}$ corresponds to the (anti-) ferromagnetic transition temperature. However, this theory does not take into account single ion effects such as the crystal field (CF) which are expected to be significant in $PuPd_3$.

There is a field-dependent residual susceptibility $\chi_0(H)$ which mainly arises from impurities, the encapsulation and the sample holder. In addition, the Pauli susceptibility of the conduction electrons may also contribute to χ_0 and can be estimated from the electronic Sommerfeld coefficient of $LuPd_3$, $\gamma_{LuPd_3}^- = 3.5(5)$ mJ mol^{-1} K^{-2}, which yields χ_{Pauli}
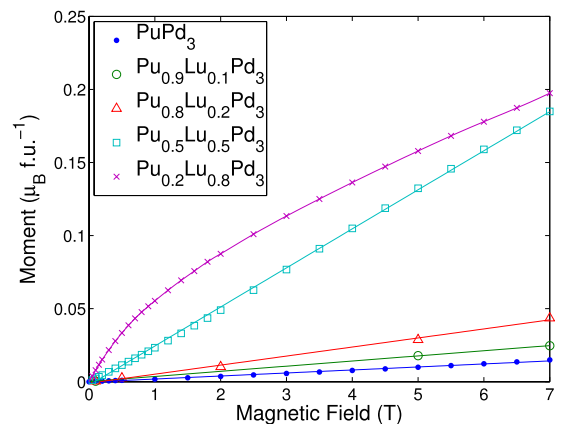

FIG. 2. (Color online) The magnetization at 2 K of $Pu_{1-x}Lu_xPd_3$. Lines are guide to the eyes.

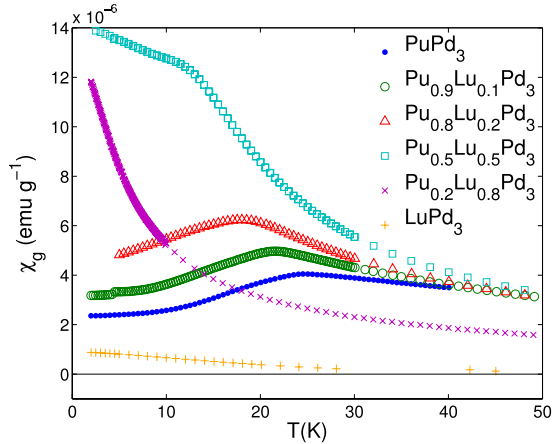FIG. 3. (Color online) The magnetic susceptibility of $Pu_{1-x}Lu_xPd_3$.

$\approx 5.2(2) \times 10^{-5}$ μ_B T^{-1} f.u.$^{-1}$. This is significantly lower than the observed values of the residual susceptibility, which are on the order of 10^{-3} μ_B T^{-1} f.u.$^{-1}$, indicating that the conduction electron susceptibility contribution is negligible. The fitted parameters to the Curie-Weiss relation for each sample are given in Table I. The quoted error is deduced from calculating the covariance matrix of the parameters from the covariance matrix of the data[6] assuming that this is diagonal and proportional to ε^{-2} where ε is the standard error in the measured moment or heat capacity as determined by the MULTIVU software supplied by Quantum Design. Figure 4 shows the inverse susceptibility of the different compositions with the residual susceptibility χ_0 subtracted.

The magnitudes of the effective moments are all significantly higher than the *LS*-coupling value, 0.85 μ_B. Any crystal-field interaction will only decrease this effective moment because as the crystal-field split levels become further
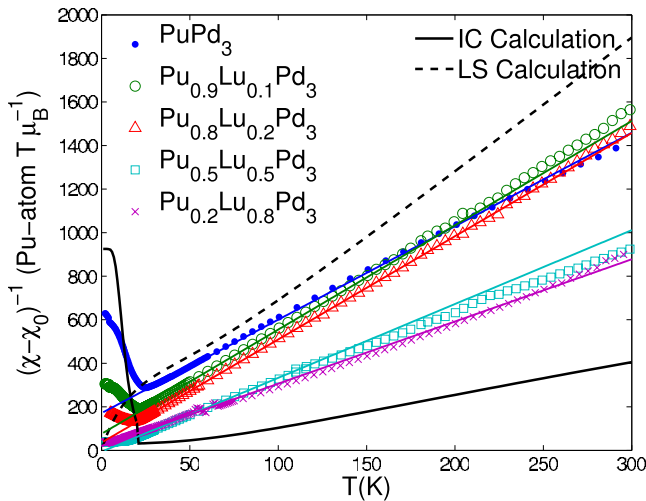

FIG. 4. (Color online) The inverse magnetic susceptibility of $Pu_{1-x}Lu_xPd_3$. Thin solid lines are fits to the modified Curie-Weiss Law for each compound. The mean-field intermediate coupling calculation is shown as a thick solid line while the dashed line shows the single ion susceptibility calculated from the crystal field in *LS* coupling.
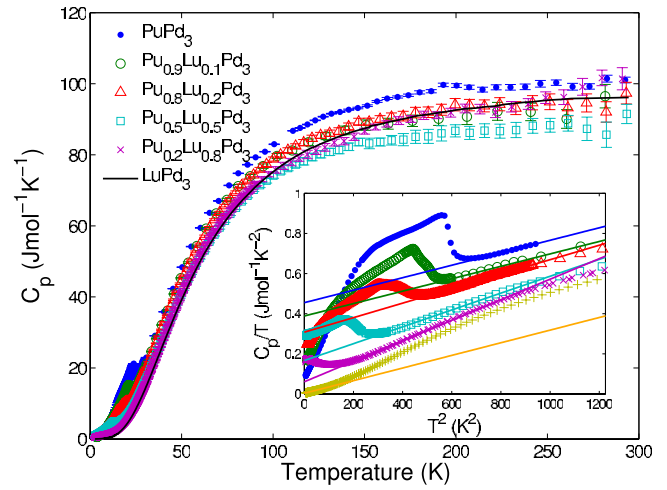

FIG. 5. (Color online) Heat capacity of $Pu_{1-x}Lu_xPd_3$ at zero applied magnetic field. The inset shows C_p/T vs T^2 and solid lines there show fits to $C/T \sim \gamma + AT^2$. LuPd$_3$ data is shown as crosses in the inset

separated and hence thermally deoccupied, their angular momentum will cease to contribute to the moment. The effective moment with zero crystal-field splitting in *intermediate coupling* on the other hand is approximately 1.4 μ_B, as calculated using the theory outlined in Sec. IV. This value may be decreased slightly by a large crystal field and suggests that we should use intermediate coupling to calculate the single-ion properties of Pu^{3+}.

An alternative reason for the higher than expected effective moment may be due to some high-moment paramagnetic impurity. However, analysis of the x-ray diffraction patterns showed that the only detectable impurity is Lu_2O_3 which is nonmagnetic. There may also be some trace amounts of oxides of Pu which is not observed in the diffraction pattern. PuO_2 is a Van Vleck paramagnet[7] which may contribute to the impurity term in Eq. (1) while Pu_2O_3 is an antiferromagnet with an effective moment of 2.1 μ_B.[8] However, one would need approximately 6 mol % Pu_2O_3 in $PuPd_3$ for it to be responsible for the increased effective moment compared to the *LS*-coupling expectation, at which concentration it should be detectable in the x-ray diffraction pattern, which is not the case. Furthermore, the enhanced value of μ_{eff} for Pu_2O_3 which also has a free ion Pu^{3+} configuration suggests that intermediate coupling is appropriate in these cases.

B. Heat capacity

The heat capacity at zero field is shown in Fig. 5 while details of the results in applied fields up to 14 T are in Fig. 6. We note that at high temperatures, C_p tends to the classical Dulong-Petit limit, $3NR = 99.8$ J mol^{-1} K^{-1}. For $Pu_{0.9}Lu_{0.1}Pd_3$, the derivative in the heat capacity shows two minima, which stem from the steplike nature of the transition. The higher temperature inflexion point at $\sim$22 K corresponds well with the peak in the inverse susceptibility but the lower temperature peak at $\sim$21 K does not match any feature in the magnetic susceptibility. Nevertheless, these two anomalies raise the possibility that there may indeed be
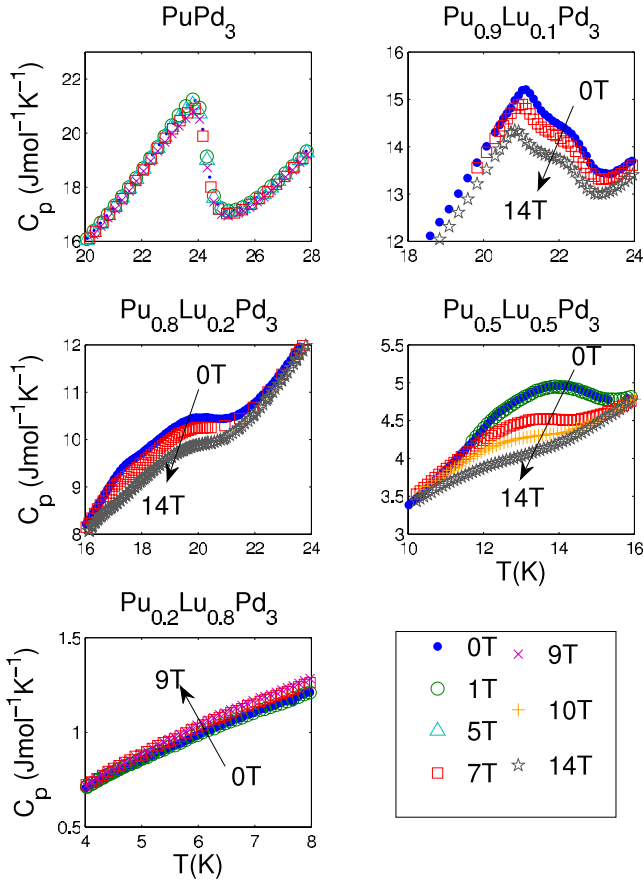
FIG. 6. (Color online) Heat capacity of $Pu_{1-x}Lu_xPd_3$ in applied magnetic field. The arrows indicate the direction of increasing field.

two transitions in this compound. Moreover, as can be seen in Fig. 6, the heat capacity of $Pu_{0.8}Lu_{0.2}Pd_3$ also shows indications of two transitions.

An estimate of the electronic specific heat $C_{el} = \gamma T$ and Debye temperature θ_D was obtained using the approximation

$$C \sim \gamma T + \frac{12\pi^4 N_A k_B}{5}\left(\frac{T^3}{\theta_D^3}\right) \tag{2}$$

which is valid at low temperatures ($T \ll \theta_D$), from a plot of C_p/T vs T^2 shown as an inset in Fig. 5. However, the magnetic heat capacity complicates the determination of γ because the Néel temperature is very low in some of the Lu-rich compounds. This increases the low temperature C_p and hence the estimate of γ from the straight line intercept. For this reason, for the Lu-rich compositions, we show the results of fitting the data in the region above T_N (γ^+) in addition to that below 8 K (γ^-) in Table I. For Pu-rich compositions, the data above T_N will be affected by the Schottky anomaly at approximately 17 K, and will be unreliable. Thus it appears from these estimates that the electronic heat capacity first increases with increasing x until $x \approx 0.5$, whereupon it falls as x rises further. The spread in the fitted parameters when data from different ranges of temperatures in the region 25 K $< T <$ 40 K for γ^+, and 2 K $< T <$ 8 K for γ^- was taken as an estimate of the errors in these parameters.
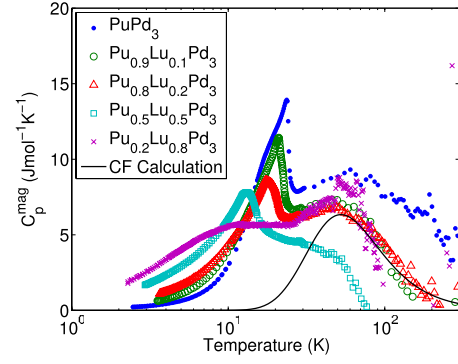

FIG. 7. (Color online) Deduced magnetic and electronic contribution to the heat capacity $C_p^{mag} = C_p(Pu_{1-x}Lu_xPd_3) - (C_p(LuPd_3) - \gamma_{Lu}^+ T)$. The solid line is a crystal-field calculation.

The Debye temperature θ_D was determined from fitting the high-temperature data, and appears to be independent of Lu doping. This suggests that the phonon contribution to the heat capacity is constant through the series. A good estimate of this contribution is given by the heat capacity of the nonmagnetic isostructural compound $LuPd_3$, which also has a negligible electronic heat capacity, $\gamma_{Lu} = 3.5(5)$ mJ mol^{-1} K^{-2}. We have thus extracted the additional electronic *and* magnetic heat capacity of $Pu_{1-x}Lu_xPd_3$ by subtracting that of $LuPd_3$, as

$$C_p^{mag} = C_p(Pu_{1-x}Lu_xPd_3) - (C_p(LuPd_3) - \gamma_{Lu}^+ T). \tag{3}$$

This extracted quantity, scaled by the Pu concentration, is shown in Fig. 7.

The magnetic heat capacity for all the compounds shows a peak at $\sim$60 K, which we attribute to a Schottky anomaly from the CF splitting. The cubic CF on the Pu^{3+} ions splits the sixfold ground multiplet ($J = \frac{5}{2}$ in LS coupling) into a doublet and quartet. The energy gap, Δ^{CF}, between these two levels determines the temperature of the Schottky peak, such that $\Delta^{CF} \sim 12$ meV corresponds to a peak at 60 K. The magnitude of this peak, however, is determined by whether the doublet ($C_p = 6.3$ J mol^{-1} K^{-1}) or quartet ($C_p = 2$ J mol^{-1} K^{-1}) is the ground state. The data in Fig. 7 thus suggest a doublet ground state.

This is supported by the magnetic entropy, shown in Fig. 8, deduced by numerically integrating the magnetic heat capacity, $S(T) = \int_2^T \frac{C_p^{mag}}{T} dT$. From the very low heat capacity of $PuPd_3$ at low temperatures, we believe the magnetic entropy from 0 to 2 K is negligible, and have not included this range in the integration. The value of the entropy at the Néel temperature is approximately $R \ln(3)$ for $PuPd_3$, which is above the value, $R \ln(2)$, expected for a doublet ground state. If the electronic heat capacity $\gamma_{Pu}^- = 76$ mJ mol^{-1} K^{-2} is subtracted from the integral, then we obtain $S(T_N) \approx R \ln(2.4)$. The remaining discrepancy may be due to (i) an incomplete subtraction of the phonon contribution, as the heat capacity of $LuPd_3$ may not be exactly analogous to the phonon heat capacity of $PuPd_3$ and (ii) a larger value of γ (see the discussion in Sec. IV).
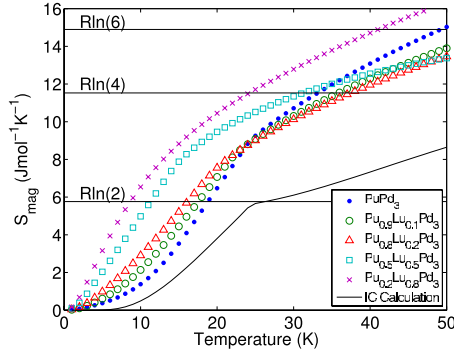
FIG. 8. (Color online) Deduced magnetic contribution to the entropy of $Pu_{1-x}Lu_xPd_3$, calculated by numerically integrating C_p^{mag}/T.

Finally, the inset to Fig. 5 shows what appears to be a hump at ~ 17 K in the heat capacity of $PuPd_3$. This feature was initially attributed to the Schottky anomaly from the CF splitting in Ref. 5. However, it is more likely due to a Schottky anomaly from the splitting of the doublet ground state in the ordered phase, and indeed such a feature is observed in the mean-field calculations in the next section. A splitting of $\Delta^{MF}=3.5$ meV gives a peak at ~ 17 K, which is reasonable.

IV. MEAN-FIELD CALCULATIONS

As noted in Sec. III A, the measured effective moment for both $PuPd_3$ and the doped compounds is approximately 1 μ_B/Pu, in contrast to the expected LS-coupling value of $g_J\sqrt{J(J+1)}=0.85$ μ_B from a Hund's rule $^6H_{5/2}$ ground state for a Pu^{3+} ion. LS coupling is a good approximation when both the Coulomb ($\mathcal{H}_C$) and spin-orbit ($\mathcal{H}_{so}$) interactions are large but $\mathcal{H}_C \gg \mathcal{H}_{so}$. In contrast, when $\mathcal{H}_C \ll \mathcal{H}_{so}$, jj-coupling is a better approximation, whereupon we obtain μ_{eff} =2.86 μ_B. In between these limits, for the case of intermediate coupling, the effective moment is a function of $\mathcal{H}_C$ and $\mathcal{H}_{so}$, and the full Hamiltonian, including both these terms and the crystal field ($\mathcal{H}_{cf}$) and Zeeman interactions ($\mathcal{H}_Z$) must be calculated.

The strength of $\mathcal{H}_C$ and $\mathcal{H}_{so}$, parameterized by the Slater (F^k) and spin-orbit (ξ) integrals, is fixed by the atomic environment of the unfilled shell electrons. Thus in practice, intermediate coupling refers to the case where the value of F^k and ξ are determined either from *ab initio* (Hartree-Fock) calculations, or from experimental measurements using optical spectroscopy. Using parameters determined experimentally by Carnall from the spectra of dilute Pu^{3+} in $LaCl_3$,[9] the effective moment is 1.44 μ_B. It is conceivable that in a metallic system such as $Pu_{1-x}Lu_xPd_3$ there may be small changes to F^k and ξ compared to the insulating salts on which the measurements of[9] were made.[10] Nevertheless, a 10% change in F^k and ξ to make the system more LS-like only yields $\mu_{eff}=1.38$ μ_B. In order to obtain $\mu_{eff}\sim 1$ μ_B, we must double the magnitude of F^k and ξ compared to their measured values, which is probably unphysical.

Given that the crystal-field interaction is small, as judged by the ~ 12 meV split between the doublet ground state and
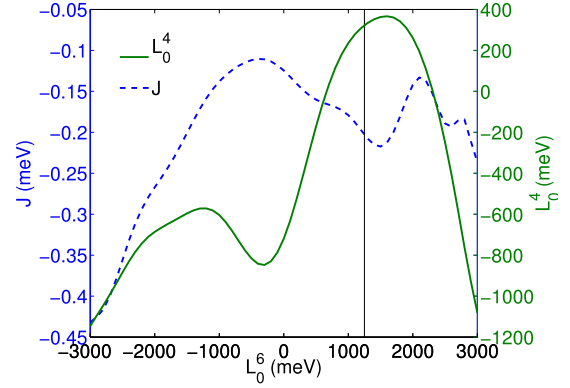

FIG. 9. (Color online) Calculated dependence of the CF parameter L_0^4 and the nearest neighbor exchange parameter $\mathcal{J}$ on L_0^6 subject to constraints described in the text. The vertical line indicates the optimal parameters.

first-excited quartet deduced from the heat capacity measurements, $\mathcal{H}_{cf}$ has little effect on μ_{eff}. Thus we believe that the lower than expected effective moment is most likely due to Kondo screening. Nonetheless, a mean field calculation which can model the antiferromagnetic order and the single ion intermediate coupling behavior is still valuable to interpret the heat capacity and magnetization data. Such a calculation, carried out using the MCPHASE package,[11] is detailed below.

We have assumed a nearest neighbor only exchange interaction between $5f$ electrons, which is reasonable given the G-type antiferromagnetic structure where nearest neighbor moments align in antiparallel. Thus, there are three free parameters in the calculations: two CF parameters, L_0^4 and L_0^6, and one exchange parameter $\mathcal{J}$. There are two other nonzero CF parameters but they are fixed by the cubic point symmetry of the Pu^{3+} ions such that $L_4^4=\sqrt{5/14}L_0^4$ and $L_4^6= -\sqrt{7/2}L_0^6$. It should be noted that the parameters used here correspond to the *Wybourne* normalization,[12] rather than the usual *Stevens* normalization (usually denoted B_l^m). This is because the Stevens operator equivalents O_l^m are valid only within a single multiplet of given J whereas we now require operators that can span all the allowed J values.

The two CF parameters are fixed by the requirement that they result in a doublet ground state with a quartet at ~ 12 meV. This fixes a relation between L_0^4 and L_0^6 as shown in Fig. 9. The Néel temperature T_N then fixes a relation between $\mathcal{J}$ and the crystal-field parameters, and finally the magnetization below T_N was used to fixed all three values, yielding $L_0^4=320$, $L_0^6=1250$, and $\mathcal{J}=-0.204$ meV.

The magnetization is calculated by including in the Hamiltonian a Zeeman term, $-\mu_B(\mathbf{L}+2\mathbf{S})\cdot\mathbf{H}$; numerically diagonalizing the energy matrix and calculating the expectation value of the moment operator $\mathbf{L}+2\mathbf{S}$. The calculated inverse susceptibility is shown as a solid black line in Fig. 4 for comparison with the measured data. Unfortunately, better agreement with the data within the constraints of the mean-field intermediate coupling model is only possible by increasing the Coulomb or spin-orbit integrals to unphysical values. A more likely explanation is the suppression of the effective moment by Kondo screening, which is not considered in the current model.
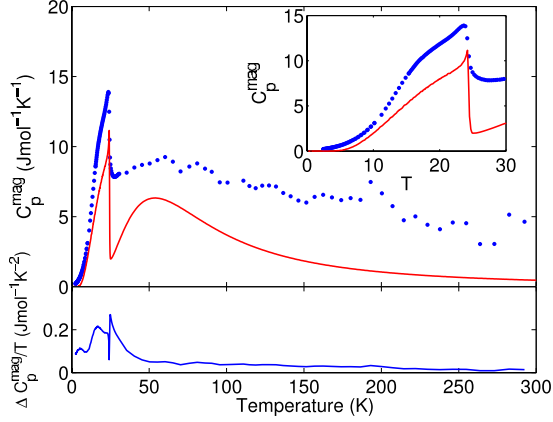
FIG. 10. (Color online) Measured and calculated magnetic heat capacity of PuPd$_3$. The estimated electronic heat capacity, $\Delta C_p^{mag}/T = \frac{C_p^{mag} - C_p^{ic}}{T}$ is given in the bottom panel and has a mean value of 122 mJ mol^{-1} K^{-2}.

The heat capacity is calculated by numerically differentiating the internal energy, $\langle U \rangle = \Sigma_n E_n \exp(-E_n/k_B T)/Z$, by the temperature, and the entropy by subsequently numerically integrating this. The calculated heat capacity, shown in Fig. 10, shows a shoulder around ~20 K in accordance with the data which arises from a Schottky peak due to the splitting of the ground state doublet in the ordered phase. We can also estimate the electronic heat capacity by subtracting this calculated C_p^{ic} from the measured electronic and magnetic heat capacity, C_p^{mag}, the result of which is shown in the bottom panel of Fig. 10. The spike near T_N is due to the differences in the sharpness of the calculated and measured transitions in this temperature range. Overall, however, the mean value, $\bar{\gamma} = 122$ mJ mol^{-1} K^{-2}, over the full temperature range is in fair agreement with that derived from the low-temperature heat capacity, $\gamma_{Pu}^- = 76$ mJ mol^{-1} K^{-2}.

Similar mean-field heat capacity calculations for the other compositions, where the exchange coupling $\mathcal{J}$ was reduced to reflect the lower T_N, did not yield the broad transitions seen in Fig. 7 but rather the sharp lambda anomalies expected of an antiferromagnetic transition. Thus a subtraction to deduce their electronic specific heat becomes increasingly untenable. The broad transitions observed in the data are probably due to disorder in the system as a result of the Lu doping.

Finally, the calculated internal fields in the model are 226 T (180 T) at 1 K (20 K), which agree well with the molecular field of 217 T determined from fitting the measured resistivity using a simple CF model, as described in the next section.

V. ELECTRICAL TRANSPORT MEASUREMENTS

Electrical transport measurements were carried out using thin parallel-sided samples extracted after crushing the polycrystalline buttons produced by arc-melting. The first transport measurements were completed some months after the production of the samples, so there were significant aging effects in the Pu samples. This prompted us to anneal the PuPd$_3$ sample, and remeasure its resistivity, resulting in a

TABLE II. Parameters for the spin-disorder resistivity model for Pu$_{1-x}$Lu$_x$Pd$_3$ described in the text. The crystal-field parameter B_4 = 0.041(1) meV was determined using the data for PuPd$_3$ and thereafter fixed in the fitting of the other compositions.

Composition	ρ_0 ($\mu\Omega$ cm)	$\rho_{s-f}^{(0)}$ ($\mu\Omega$ cm)	B_{mf} (T)	B_{mf}^{ic} (T)
PuPd$_3$	12.0(1)	876(37)	217(23)	226
Pu$_{0.9}$Lu$_{0.1}$Pd$_3$	75(1)	118(5)	88(4)	149
Pu$_{0.8}$Lu$_{0.2}$Pd$_3$	97(1)	35(1)	213(6)	143
Pu$_{0.5}$Lu$_{0.5}$Pd$_3$	172(1)	53(2)	92(5)	129
Pu$_{0.2}$Lu$_{0.8}$Pd$_3$	11.5(1)	17.8(1)	51(1)	88

large decrease in the residual resistivity ρ_0 from 225 to 11 $\mu\Omega$ cm. Subsequently the resistivity of the other compositions was also remeasured after annealing. The values of ρ_0 show a rapid increase with Lu doping up to $x=0.5$ thereafter decreasing with x, as summarized in Table II. This is due to the increasing number of defects caused by Lu substitution. Finally, measurements of the Hall coefficient and longitudinal resistivity of PuPd$_3$ and the $x=0.1, 0.2, 0.5$ compositions in field were also carried out.

The resistivity of LuPd$_3$ is well fitted by the Bloch-Grüneisen relation

$$\rho = C \frac{T^5}{\theta_D^6} \int_0^x \frac{x^5}{(e^x - 1)(1 - e^{-x})} dx, \qquad (4)$$

where $x = T/\theta_D$, with $C = 181(1)$ $\mu\Omega$ cm and $\theta_D = 166(1)$ K. It was taken to be representative of the nonmagnetic contribution to the resistivity of Pu$_{1-x}$Lu$_x$Pd$_3$, and used to estimate the magnetic resistivity as $\Delta\rho = \rho(Pu_{1-x}Lu_xPd_3) - \rho(LuPd_3)$. This quantity is plotted in the case of zero applied magnetic field in Fig. 11. The in-field measurements showed little change from the zero field data, and the data for PuPd$_3$ agree well with previous measurements,[13] albeit with a slightly lower residual resistivity.
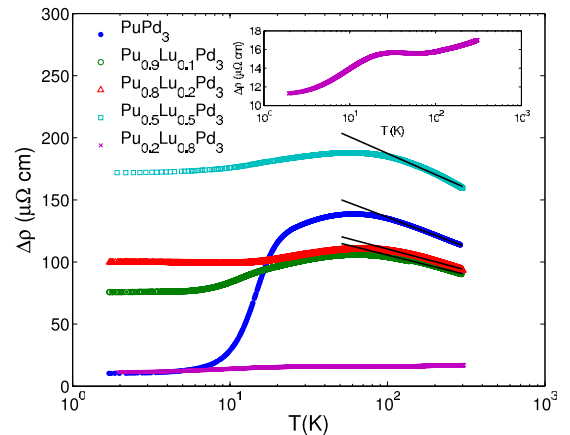

FIG. 11. (Color online) Zero-field magnetic resistivity of (Pu,Lu)Pd$_3$ on a logarithmic scale. Inset is an enlarged view of the Pu$_{0.2}$Lu$_{0.8}$Pd$_3$ composition. Solid lines are fits to the relation $\rho_0 - \rho_1 \log(T)$ described in the text.

Qualitatively, the behavior of the resistivity may be divided into a high-temperature Kondo-type regime, where the resistivity increases with decreasing temperature until ∼50 K, followed by the onset of coherence, from where it falls sharply with temperature, and shows no clear anomaly at T_N. At low temperatures, the resistivity follows an exponential temperature behavior, in contrast to the power-law behavior expected in metals from the Bloch-Grüneisen relation. Electrons scattering from antiferromagnetic magnons will give rise to an exponential temperature dependence, as will spin-disorder scattering from the localized $5f$ moments themselves. A fit to the electron-magnon resistivity[14] assuming an isotropic magnon dispersion $\omega = \sqrt{\Delta^2 + Dk^2}$, such that[15]

$$\rho_{e-m} = \rho_0 + B\Delta^2 \sqrt{\frac{k_B T}{\Delta}} e^{-\Delta/k_B T} \left[1 + \frac{3\Delta}{2k_B T} + \frac{2}{15}\left(\frac{\Delta}{k_B T}\right)^2 \right] \tag{5}$$

yields, however, a spin-gap $\Delta = 4$ meV which is significantly larger than that expected from the heat capacity below T_N, if the shoulder at 17 K corresponds to a Schottky peak which arises from a gap of approximately 3.2 meV. In contrast, this very splitting between the doublet ground states in the ordered phase is predicted by the spin-disorder resistivity model described below.

Above ∼70 K, the resistivity is well fitted by a $\rho_0 - \rho_1 \log(T)$ term,[16] where ρ_0 is the residual resistivity, and ρ_1 is proportional to the interaction between the conduction electrons and Kondo impurities. The fit is shown in Fig. 11, with parameters $\rho_0 = 235.8(3)$ $\mu\Omega$ cm and $\rho_1 = 22(1)$ $\mu\Omega$ cm for PuPd$_3$. The value of ρ_1 initially decreases with Lu doping to 15(2) $\mu\Omega$ cm for $x=0.1$ and 16(2) $\mu\Omega$ cm for $x=0.2$ but then increases to 27(3) $\mu\Omega$ cm for $x=0.5$. This increase suggests that the Kondo interaction is strengthened at half doping.

The magnetic resistivity of Pu$_{0.2}$Lu$_{0.8}$Pd$_3$ does not show the Kondo behavior of the other compositions but rather increases with increasing temperature with a plateau region around 30–80 K. This behavior and also the exponential temperature dependence of the low-temperature part of the resistivity is characteristic of a simple crystal field spin-disorder resistivity model.[17] This model is based on the scattering of conduction electrons with spin **s** by a localized moment **J** through an exchange interaction $-2G\mathbf{s} \cdot \mathbf{J}$, giving the resistivity in the first Born approximation as

$$\rho_{\text{s-f}} = \frac{3\pi N m^*}{\hbar e^2 E_F} G^2 (g-1)^2 \frac{1}{Z}$$
$$\times \sum_{m_s, m'_s, i, i'} \langle m'_s, \psi'_i | \mathbf{s} \cdot \mathbf{J} | m_s, \psi_i \rangle p_i f_{ii'}, \tag{6}$$

where the occupation factor for the crystal-field level at E_i is $p_i = \exp(-\frac{E_i}{k_B T})$ and the conduction electron population factor is $f_{ii'} = 2[1 + \exp(-\frac{E_i - E_{i'}}{k_B T})]^{-1}$. The wave functions $|\psi_i\rangle$ and energies E_i are determined by diagonalising the crystal-field Hamiltonian.
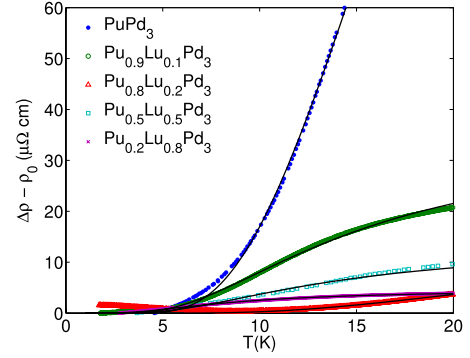

FIG. 12. (Color online) Zero-field magnetic resistivity of (Pu,Lu)Pd$_3$ with residual resistivity ρ_0 subtracted. Solid lines are fits using the crystal-field model described in the text

In the absence of a crystal field, the $2J+1$ degenerate spin orbit ground-state levels yield a temperature-independent resistivity given by

$$\rho_{\text{s-f}}^{(0)} = \frac{3\pi N m^*}{\hbar e^2 E_F} G^2 (g-1)^2 J(J+1). \tag{7}$$

In our case, with a $J = \frac{5}{2}$ multiplet in a cubic crystal field, and in the absence of a magnetic field, Eq. (6) reduces to a sum of exponential functions because the wave functions $|\psi_i\rangle$ are fixed, and the crystal-field parameter can only change the splitting Δ^{CF} between the quartet and doublet. There is thus a universal behavior, with the resistivity tending to $\rho_{\text{s-f}}^{(0)}$ at $T \gg \Delta^{\text{CF}}$, and then falling exponentially as the temperature falls below some level such that the excited crystal-field states are no longer populated. This temperature is approximately $0.4\Delta^{\text{CF}}$, so the model suggests a splitting $\Delta^{\text{CF}} \approx 3.2$ meV, as the drop off in resistivity occurs around 15 K. This is significantly smaller than the splitting deduced from the Schottky peak at ∼60 K but is similar to the splitting of the ground-state doublet (Δ^{MF}) in the ordered phase, as determined by the shoulder at ∼17 K in the heat capacity data.

In order to accommodate this splitting, we introduce a molecular field B_{mf} term. The low-temperature exponential increase is then governed primarily by the split doublet, with a second exponential step at higher temperatures due to the crystal-field splitting. It turns out that this second step is not observed in the case of PuPd$_3$ because the two steps merge into each other. Indeed a fit to the data below T_N with all parameters in the spin-disorder resistivity model varying freely yields a CF splitting of 14 meV, in agreement with the heat capacity data. As B_{mf} decreases in line with T_N with increasing Lu doping while the CF splitting remains constant, the two steps become more pronounced in the calculations. These two steps are observed in the case of Pu$_{0.2}$Lu$_{0.8}$Pd$_3$ but the second step is masked by the Kondo screening in the other compositions.

Using this simple crystal-field model we obtained the parameters shown in Table II. Figure 12 shows the resulting fit to the data with ρ_0 subtracted. The CF splitting was fixed for all Lu-doped compositions to the value determined from fitting the PuPd$_3$ data. The molecular field determined from mean-field calculations, $B_{\text{mf}}^{\text{ic}}$, with exchange parameters $\mathcal{J} =$
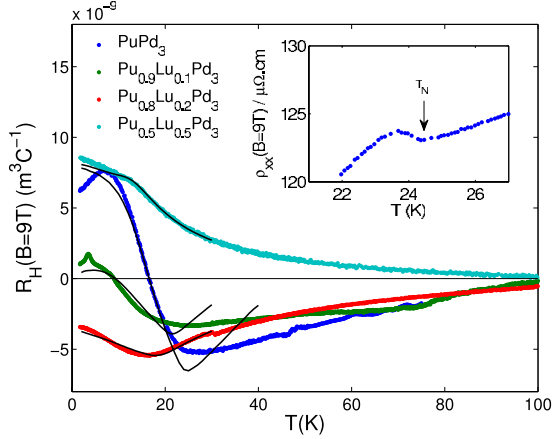
FIG. 13. (Color online) Temperature dependence of the Hall coefficient $R_H = \rho_{xy}/B$ and magnetoresistance at 9 T (inset). The solid black line is a fit using the measured magnetic susceptibility as described in the text

TABLE III. Fitted Hall constants of $Pu_{1-x}Lu_xPd_3$. All values are in (10^{-9} m^3 C^{-1}).

$x=$	0	0.1	0.2	0.5
R_0	32.9(4)	12.1(2)	1.5(1)	0.9(1)
R_1	−6.97(8)	−2.31(3)	−0.74(1)	−0.028(1)

The temperature dependence of the Hall effect may be described phenomenologically by a scaling of the magnetization, as in

$$\rho_{xy}(T) = R_0 B + R_1 \mu_0 M(T), \tag{8}$$

where R_0 is the *ordinary* and R_1 the *extraordinary* Hall constant. In Fig. 13, the solid lines show fits of the Hall coefficient to this relation using the measured magnetization data. Both the ordinary and extraordinary Hall constants were found to decrease with Lu doping, as shown in Table III. R_1 is proportional to the conduction-f electron exchange interaction strength G discussed above, so the decrease in its magnitude further indicates that this interaction becomes weaker with Lu doping.

Finally, we observed that the magnetoresistance, $\rho(B)$, is linear with applied field for all samples and showed a negative slope at high temperatures and a positive slope at low temperatures, except for LuPd$_3$ where the slope was always positive. We interpret the negative magnetoresistance to be a sign of the Kondo effect at high temperatures with the normal metallic behavior giving a positive magnetoresistance at low temperatures.

−0.202 meV, −0.199 meV, −0.1925 meV, and −0.174 meV, for compositions $x=0.1$, 0.2, 0.5, and 0.8, respectively, is also shown in the table. Apart from the case of Pu$_{0.8}$Lu$_{0.2}$Pd$_3$, the fitted B_{mf} is consistently lower than the calculated B_{mf}^{ic}. This is due to the overestimation of T_N in the mean-field approximation because we have estimated $\mathcal{J}$ from T_N, and B_{mf}^{ic} is proportional to $\mathcal{J}$. Thus, B_{mf}^{ic} is also overestimated.

Pu$_{0.8}$Lu$_{0.2}$Pd$_3$ shows an upturn at low temperatures, which cannot be accounted for by the current model. In addition, this upturn affects the fit by decreasing the ratio between the maximum and minimum resistivity, and hence $\rho_{s-f}^{(0)}$. The exponential increase in the resistivity also occurs at a higher temperature and over a broader temperature range in this composition than in the others, which explains the anomalously high B_{mf}. These features may be artifacts of the sample, because while an aged Pu$_{0.9}$Lu$_{0.1}$Pd$_3$ showed the upturn at low temperatures, the annealed sample did not whereas both aged and annealed Pu$_{0.8}$Lu$_{0.2}$Pd$_3$ samples showed the upturn. Furthermore the resistivity of the aged Pu$_{0.8}$Lu$_{0.2}$Pd$_3$ sample is lower than that of the annealed sample. This suggests that the annealing had not fully repaired the radiation damage, and thus the resistivity may be strongly affected by crystallographic defects.

Nevertheless when the fits were repeated using the calculated B_{mf}^{ic} as fixed parameters, the fitted $\rho_{s-f}^{(0)}$ changed by less than 10%. The fits thus showed that the f-conduction electron interaction decreases with Lu doping with a slight increase for the $x=0.5$ composition compared to $x=0.2$ and $x=0.8$, in agreement with the fits to the Kondo parameter ρ_1.

We now turn to the electrical transport properties in an applied magnetic field. The temperature dependence of the Hall coefficient R_H and the magnetoresistivity ρ_{xx} in 9 T are shown in Fig. 13. $\rho_{xx}(T)$ follows the same behavior as the zero field resistivity shown above, with the exception that there is a small peak just below the Néel temperature as shown in the inset to the figure. This was not observed previously and is reminiscent of the superzone scattering near T_N in the heavy rare earths.[18]

VI. CONCLUSIONS

We have completed extensive bulk properties measurements on antiferromagnetic PuPd$_3$ and the pseudobinary compounds Pu$_{1-x}$Lu$_x$Pd$_3$. The transition temperature was found to decrease linearly from $T_N=24.4(3)$ K in PuPd$_3$ to 7(2) K in Pu$_{0.2}$Lu$_{0.8}$Pd$_3$.

Heat capacity measurements show a Schottky anomaly at ~60 K, which was interpreted as arising from a crystal-field splitting between a doublet ground state and an excited state quartet at ~12 meV. The deduced Sommerfeld coefficient, γ was found to be significantly higher than that expected for the free-electron model, with a value on the order of 0.1 J mol^{-1} K^{-2} determined by fitting the data directly and by subtracting the calculated magnetic and measured phonon contributions. Direct fits to the data suggest that γ decreases with increasing Lu substitution. The magnetic heat capacity was calculated using a mean field model which showed that the shoulder in the data corresponds to a splitting of the doublet ground state in the ordered phase with a gap of ~3.5 meV. The size of this gap is supported by fits of the resistivity to a crystal-field model.

Magnetic susceptibility and magnetization measurements also showed that the paramagnetic effective moment, μ_{eff} increases with Lu concentration, approaching the value expected in intermediate coupling. These observations arise from the Kondo interaction which suppresses the effective

magnetic moment but enhances the electronic effective mass, m^*. As the Kondo interaction decreases with Lu doping, μ_{eff} is screened less, and $\gamma \propto m^*$ falls.

Electrical transport measurements support this decrease in the Kondo interaction with increasing Lu concentration, x, as parameters proportional to the f-conduction electron coupling in a crystal field model of the resistivity and Hall effect were found to fall as x increases.

ACKNOWLEDGMENTS

We thank G. H. Lander and K. Gofryk for helpful discus-

*duc.le@helmholtz-berlin.de

[1] H. C. Walker, K. A. McEwen, M. D. Le, L. Paolasini, and D. Fort, J. Phys.: Condens. Matter **20**, 395221 (2008).

[2] H. C. Walker, K. A. McEwen, P. Boulet, E. Colineau, J.-C. Griveau, J. Rebizant, and F. Wastin, Phys. Rev. B **76**, 174437 (2007).

[3] M. D. Le, H. C. Walker, K. A. McEwen, T. Gouder, F. Huber, and F. Wastin, J. Phys.: Condens. Matter **20**, 275220 (2008).

[4] W. J. Nellis, A. R. Harvey, G. H. Lander, B. D. Dunlap, M. B. Brodsky, M. H. Mueller, J. F. Reddy, and G. R. Davidson, Phys. Rev. B **9**, 1041 (1974).

[5] M. D. Le, K. A. McEwen, F. Wastin, P. Boulet, E. Colineau, R. Jardin, and J. Rebizant, Physica B **403**, 1035 (2008).

[6] Y. Bard, *Nonlinear Parameter Estimation* (Academic Press, New York, 1974).

[7] G. Raphael and R. Lallement, Solid State Commun. **6**, 383 (1968).

[8] B. McCart, G. H. Lander, and A. T. Aldred, J. Chem. Phys. **74**, 5263 (1981).

[9] W. T. Carnall, J. Chem. Phys. **96**, 8713 (1992).

[10] A. D. Taylor, R. Osborn, K. A. McEwen, W. G. Stirling, Z. A. Bowden, W. G. Williams, E. Balcar, and S. W. Lovesey, Phys. Rev. Lett. **61**, 1309 (1988).

[11] M. Rotter, J. Magn. Magn. Mater. **272-276**, E481 (2004).

[12] D. J. Newman and B. K. C. Ng, *Crystal Field Handbook* (Cambridge University Press, Cambridge, England, 2000).

[13] A. R. Harvey, M. B. Brodsky, and W. J. Nellis, Phys. Rev. B **7**, 4137 (1973).

[14] N. Hessel Andersen and H. Smith, Phys. Rev. B **19**, 384 (1979).

[15] K. Gofryk, J.-C. Griveau, E. Colineau, and J. Rebizant, Phys. Rev. B **77**, 092405 (2008).

[16] J. Kondo, Prog. Theor. Phys. **32**, 37 (1964).

[17] V. U. S. Rao and W. E. Wallace, Phys. Rev. B **2**, 4613 (1970).

[18] A. R. Mackintosh, Phys. Lett. **4**, 140 (1963).